4.10

CONFORMAL MAPPING METHODS FOR INTERFACIAL DYNAMICS

Martin Z. Bazant[1] and Darren Crowdy[2]
[1]*Department of Mathematics, Massachusetts Institute of Technology, Cambridge, MA, USA*
[2]*Department of Mathematics, Imperial College, London, UK*

Microstructural evolution is typically beyond the reach of mathematical analysis, but in two dimensions certain problems become tractable by complex analysis. Via the analogy between the geometry of the plane and the algebra of complex numbers, moving free boundary problems may be elegantly formulated in terms of conformal maps. For over half a century, conformal mapping has been applied to continuous interfacial dynamics, primarily in models of viscous fingering and solidification. Current developments in materials science include models of void electro-migration in metals, brittle fracture, and viscous sintering. Recently, conformal-map dynamics has also been formulated for stochastic problems, such as diffusion-limited aggregation and dielectric breakdown, which has re-invigorated the subject of fractal pattern formation.

Although restricted to relatively simple models, conformal-map dynamics offers unique advantages over other numerical methods discussed in this chapter (such as the Level–Set Method) and in Chapter 9 (such as the phase field method). By absorbing all geometrical complexity into a time-dependent conformal map, it is possible to transform a moving free boundary problem to a simple, static domain, such as a circle or square, which obviates the need for front tracking. Conformal mapping also allows the exact representation of very complicated domains, which are not easily discretized, even by the most sophisticated adaptive meshes. Above all, however, conformal mapping offers analytical insights for otherwise intractable problems.

After reviewing some elementary concepts from complex analysis in Section 1, we consider the classical application of conformal mapping methods to continuous-time interfacial free boundary problems in Section 2. This includes cases where the governing field equation is harmonic, biharmonic, or in a more general conformally invariant class. In Section 3, we discuss the

S. Yip (ed.),
Handbook of Materials Modeling. Volume I: Methods and Models, 1–35.

recent use of random, iterated conformal maps to describe analogous discrete-time phenomena of fractal growth. Although most of our examples involve planar domains, we note in Section 4 that interfacial dynamics can also be formulated on curved surfaces in terms of more general conformal maps, such as stereographic projections. We conclude in Section 5 with some open questions and an outlook for future research.

1. Analytic Functions and Conformal Maps

We begin by reviewing some basic concepts from complex analysis found in textbooks such as Churchill and Brown [1]. For a fresh geometrical perspective, see Needham [2].

A general function of a complex variable depends on the real and imaginary parts, x and y, or, equivalently, on the linear combinations, $z = x + iy$ and $\bar{z} = x - iy$. In contrast, an *analytic function*, which is differentiable in some domain, can be written simply as $w = u + iv = f(z)$. The condition, $\partial f/\partial \bar{z} = 0$, is equivalent to the Cauchy–Riemann equations,

$$\frac{\partial u}{\partial x} = \frac{\partial v}{\partial y} \quad \text{and} \quad \frac{\partial u}{\partial y} = -\frac{\partial v}{\partial x}, \tag{1}$$

which follow from the existence of a unique derivative,

$$f' = \frac{\partial f}{\partial x} = \frac{\partial u}{\partial x} + i\frac{\partial v}{\partial x} = \frac{\partial f}{\partial (iy)} = \frac{\partial v}{\partial y} - i\frac{\partial u}{\partial y}, \tag{2}$$

whether taken in the real or imaginary direction.

Geometrically, analytic functions correspond to special mappings of the complex plane. In the vicinity of any point where the derivative is nonzero, $f'(z) \neq 0$, the mapping is locally linear, $\mathrm{d}w = f'(z)\,\mathrm{d}z$. Therefore, an infinitesimal vector, $\mathrm{d}z$, centered at z is transformed into another infinitesimal vector, $\mathrm{d}w$, centered at $w = f(z)$ by a simple complex multiplication. Recalling Euler's formula, $(r_1 e^{i\theta_1})(r_2 e^{i\theta_2}) = (r_1 r_2) e^{i(\theta_1 + \theta_2)}$, this means that the mapping causes a local stretch by $|f'(z)|$ and local rotation by $\arg f'(z)$, regardless of the orientation of $\mathrm{d}z$. As a result, an analytic function with a nonzero derivative describes a *conformal mapping* of the plane, which preserves the angle between any pair of intersecting curves. Intuitively, a conformal mapping smoothly warps one domain into another with no local distortion.

Conformal mapping provides a very convenient representation of free boundary problems. The Riemann Mapping Theorem guarantees the existence of a unique conformal mapping between any two simply connected domains, but the challenge is to derive its dynamics for a given problem. The only constraint is that the conformal mapping be *univalent*, or one-to-one, so that physical fields remain single-valued in the evolving domain.

2. Continuous Interfacial Dynamics

2.1. Harmonic Fields

Most applications of conformal mapping involve *harmonic* functions, which are solutions to Laplace's equation,

$$\nabla^2\phi = 0. \tag{3}$$

From Eq. (1), it is easy to show that the real and imaginary parts of an analytic function are harmonic, but the converse is also true: Every harmonic function is the real part of an analytic function, $\phi = \mathrm{Re}\,\Phi$, the *complex potential*.

This connection easily produces new solutions to Laplace's equation in different geometries. Suppose that we know the solution, $\phi(w) = \mathrm{Re}\,\Phi(w)$, in a simply connected domain in the w-plane, Ω_w, which can be reached by conformal mapping, $w = f(z,t)$, from another, possibly time-dependent domain in the z-plane, $\Omega_z(t)$. A solution in $\Omega_z(t)$ is then given by

$$\phi(z,t) = \mathrm{Re}\,\Phi(w) = \mathrm{Re}\,\Phi(f(z,t)) \tag{4}$$

because $\Phi(f(z))$ is also analytic, with a harmonic real part. The only caveat is that the boundary conditions be invariant under the mapping, which holds for Dirichlet ($\phi = \text{constant}$) or Neumann ($\hat{\boldsymbol{n}} \cdot \nabla\phi = 0$) conditions. Most other boundary conditions invalidate Eq. (4) and thus complicate the analysis.

The complex potential is also convenient for calculating the gradient of a harmonic function. Using Eqs. (1) and (2), we have

$$\nabla_z\phi = \frac{\partial\phi}{\partial x} + i\frac{\partial\phi}{\partial y} = \overline{\Phi'}, \tag{5}$$

where ∇_z is the complex gradient operator, representing the vector gradient, ∇, in the z-plane.

2.1.1. Viscous fingering and solidification

The classical application of conformal-map dynamics is to *Laplacian growth*, where a free boundary, $B_z(t)$, moves with a (normal) velocity,

$$\mathbf{v} = \frac{\mathrm{d}z}{\mathrm{d}t} \propto \nabla\phi, \tag{6}$$

proportional to the gradient of a harmonic function, ϕ, which vanishes on the boundary [3]. Conformal mapping for Laplacian growth was introduced independently by Polubarinova–Kochina and Galin in 1945 in the context of ground-water flow, where ϕ is the pressure field and $\mathbf{u} = (k/\eta)\nabla\phi$ is the velocity of the fluid of viscosity, η, in a porous medium of permeability, k, according

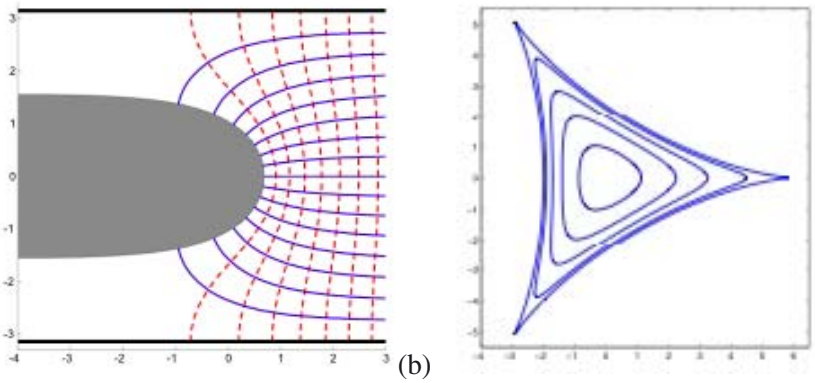

Figure 1. Exact solutions for Laplacian growth, a simple model of viscous fingering: (a) a Saffman–Taylor finger translating down an infinite channel, showing iso-pressure curves (dashed) and streamlines (solid) in the viscous fluid, and (b) the evolution of a perturbed circular bubble leading to cusp singularities in finite time. (Courtesy of Jaehyuk Choi.)

to Darcy's law. Laplace's equation follows from incompressibility, $\nabla \cdot \mathbf{u} = 0$. The free boundary represents an interface with a less viscous, immiscible fluid at constant pressure, which is being forced into the more viscous fluid.

In physics, Laplacian growth is viewed as a fundamental model for pattern formation. It also describes viscous fingering in Hele–Shaw cells, where a bubble of fluid, such as air, displaces a more viscous fluid, such as oil, in the narrow gap between parallel flat plates. In that case, the depth averaged velocity satisfies Darcy's law in two dimensions. Laplacian growth also describes dendritic solidification in the limit of low undercooling, where ϕ is the temperature in the melt [4].

To illustrate the derivation of conformal-map dynamics, let us consider viscous fingering in a channel with impenetrable walls, as shown in Fig. 1(a). The viscous fluid domain, $\Omega_z(t)$, lies in a periodic horizontal strip, to the right of the free boundary, $B_z(t)$, where uniform flow of velocity, U, is assumed far ahead of the interface. It is convenient to solve for the conformal map, $z = g(w, t)$, to this domain from a half strip, $\mathrm{Re}\, w > 0$, where the pressure is simply linear, $\phi = \mathrm{Re}\, Uw/\mu$. We also switch to dimensionless variables, where length is scaled to a characteristic size of the initial condition, L, pressure to UL/μ, and time to L/U.

Since $\nabla_w \phi = 1$ in the half strip, the pressure gradient at a point, $z = g(w, t)$, on the physical interface is easily obtained from Eq. (30):

$$\nabla_z \phi = \overline{\frac{\partial f}{\partial z}} = \left(\overline{\frac{\partial g}{\partial w}} \right)^{-1} \tag{7}$$

where $w = f(z,t)$ is the inverse mapping (which exists as long as the mapping remains univalent). Now consider a Lagrangian marker, $z(t)$, on the interface, whose pre-image, $w(t)$, lies on the imaginary axis in the w-plane. Using the chain rule and Eq. (7), the kinematic condition, Eq. (6), becomes,

$$\frac{\mathrm{d}z}{\mathrm{d}t} = \frac{\partial g}{\partial t} + \frac{\partial g}{\partial w}\frac{\mathrm{d}w}{\mathrm{d}t} = \left(\overline{\frac{\partial g}{\partial w}}\right)^{-1}. \tag{8}$$

Multiplying by $\overline{\partial g/\partial w} \neq 0$, this becomes

$$\overline{\frac{\partial g}{\partial w}}\frac{\partial g}{\partial t} + \left|\frac{\partial g}{\partial w}\right|^2 \frac{\mathrm{d}w}{\mathrm{d}t} = 1. \tag{9}$$

Since the pre-image moves along the imaginary axis, $\mathrm{Re}(\mathrm{d}w/\mathrm{d}t) = 0$, we arrive at the *Polubarinova–Galin equation* for the conformal map:

$$\mathrm{Re}\left(\overline{\frac{\partial g}{\partial w}}\frac{\partial g}{\partial t}\right) = 1, \quad \text{for } \mathrm{Re}\, w = 0. \tag{10}$$

From the solution to Eq. (10), the pressure is given by $\phi = \mathrm{Re}\, f(z,t)$. Note that the interfacial dynamics is nonlinear, even though the quasi-steady equations for ϕ are linear.

The best-known solutions are the Saffman–Taylor fingers,

$$g(w,t) = \frac{t}{\lambda} + w + 2(1-\lambda)\log(1+e^{-w}) \tag{11}$$

which translate at a constant velocity, λ^{-1}, without changing their shape [5]. Note that (11) is a solution to the fingering problem for all choices of the parameter λ. This parameter specifies the finger width and can be chosen arbitrarily in the solution (11). In experiments however, it is found that the viscous fingers that form are well fit by a Saffman–Taylor finger filling precisely half of the channel, that is with $\lambda = 1/2$, as shown in Fig. 1(a). Why this happens is a basic problem in *pattern selection*, which has been the focus of much debate in the literature over the last 25 years.

To understand this problem, note that the viscous finger solutions (11) do not include any of the effects of surface tension on the interface between the two fluids. The intriguing pattern selection of the $\lambda = 1/2$ finger has been attributed to a singular perturbation effect of small surface tension. Surface tension, γ, is a significant complication because it is described by a non-conformally-invariant boundary condition,

$$\phi = \gamma\,\kappa, \quad \text{for } z \in B_z(t) \tag{12}$$

where κ is the local interfacial curvature, entering via the Young–Laplace pressure. Small surface tension can be treated analytically as a singular perturbation to gain insights into pattern selection [6, 7]. Since surface tension

effects are only significant at points of high curvature κ in the interface, and given that the finger in Fig. 1(a) is very smooth with no such points of high curvature, it is surprising that surface tension acts to select the finger width. Indeed, the viscous fingering problem has been shown to be full of surprises [8].

In a radial geometry, the univalent mapping is from the exterior of the unit circle, $|\omega| = 1$, to the exterior of a finite bubble penetrating an infinite viscous liquid. Bensimon and Shraiman [9] introduced a *pole dynamics* formulation, where the map is expressed in terms of its zeros and poles, which must lie inside the unit circle to preserve univalency. They showed that Laplacian growth in this geometry is ill-posed, in the sense that cusp-like singularities occur in finite time (as a zero hits the unit circle) for a broad class of initial conditions, as illustrated in Fig. 1(b). (See Howison [3] for a simple, general proof due to Hohlov.) This initiated a large body of work on how Laplacian growth is "regularized" by surface tension or other effects in real systems.

Despite the analytical complications introduced by surface tension, several exact steady solutions with non-zero surface tension are known [10, 11]. Surface tension can also be incorporated into numerical simulations based on the same conformal-mapping formalism [12], which show how cusps are avoided by the formation of new fingers [13]. For example, consider a three-fold perturbation of a circular bubble, whose exact dynamics without surface tension is shown in Fig. 1(b). With surface tension included, the evolution is very similar until the cusps begin to form, at which point the tips bulge outward and split into new fingers, as shown in Fig. 2. This process repeats itself to produce a complicated fractal pattern [14], which curiously resembles the diffusion-limited particle aggregates discussed below in Section 3.

2.1.2. Density-driven instabilities in fluids

An important class of problems in fluid mechanics involves the nonlinear dynamics of an interface between two immiscible fluids of different densities. In the presence of gravity, there are some familiar cases. Deep-water waves involve finite disturbances (such as steady "Stokes waves") in the interface between lighter fluid (air) over a heavier fluid (water). With an inverted density gradient, the Rayleigh–Taylor instability develops when a heavier fluid lies above a lighter fluid, leading to large plumes of the former sinking into the latter. Tanveer [15] has used conformal mapping to analyze the Rayleigh–Taylor instability and has provided evidence to associate the formation of plumes with the approach of various conformal mapping singularities to the unit circle.

A related problem is the Richtmyer–Meshkov instability, which occurs when a shock wave passes through an interface between fluids of different

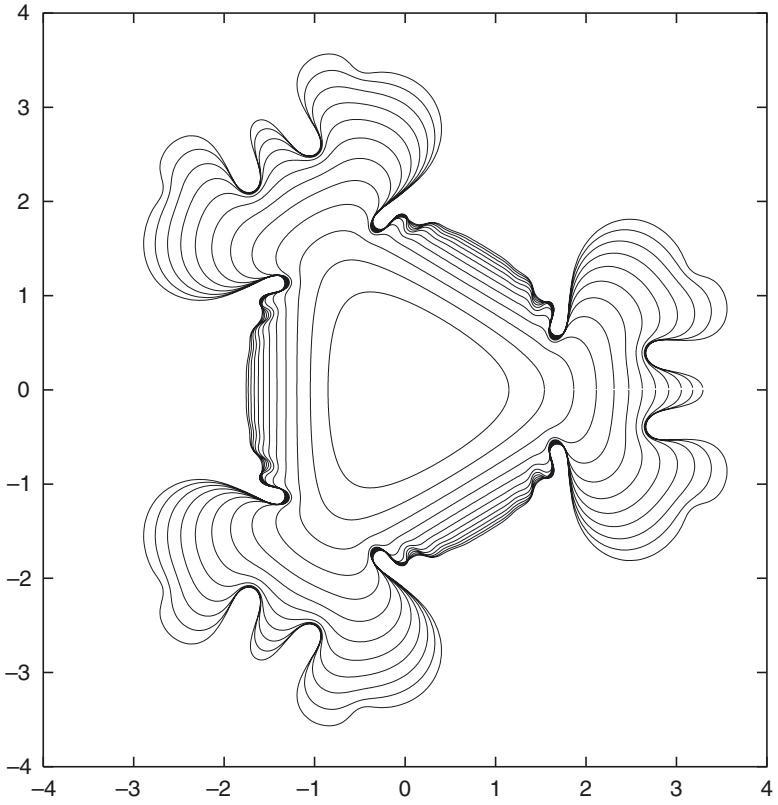

Figure 2. Numerical simulation of viscous fingering, starting from a three-fold perturbation of a circular bubble. The only difference with the Laplacian-growth dynamics in Fig. 1(b) is the inclusion of surface tension, which prevents the formation of cusp singularities. (Courtesy of Michael Siegel.)

densities. Behind the shock, narrow fingers of the heavier fluid penetrate into the lighter fluid. The shock wave usually passes so quickly that compressibility only affects the onset of the instability, while the nonlinear evolution occurs much faster than the development of viscous effects. Therefore, it is reasonable to assume a potential flow in each fluid region, with randomly perturbed initial velocities. Although real plumes roll up in three dimensions and bubbles can form, conformal mapping in two dimensions still provides some insights, with direct relevance for shock tubes of high aspect ratio.

A simple conformal-mapping analysis is possible for the case of a large density contrast, where the lighter fluid is assumed to be at uniform pressure. The Richtmyer–Meshkov instability (zero-gravity limit) is then similar to the Saffman–Taylor instability, except that the total volume of each fluid is fixed. A periodic interface in the y direction, analogous to the channel geometry

in Fig. 1, can be described by the univalent mapping, $z = g(w, t)$, from the interior of the unit circle in the mathematical w plane to the interior of the heavy-fluid finger in the physical z-plane.

Zakharov [16] introduced a Hamiltonian formulation of the interfacial dynamics in terms of this conformal map, taking into account kinetic and potential energy, but not surface tension. One way to derive equations of motion is to expand the map in a *Taylor series*,

$$g(w, t) = \log w + \sum_{n=0}^{\infty} a_n(t) w^n, \quad |w| < 1. \tag{13}$$

(The $\log w$ term first maps the disk to a periodic half strip.) On the unit circle, $w = e^{i\theta}$, the pre-image of the interface, this is simply a complex Fourier series. The Taylor coefficients, $a_n(t)$, act as generalized coordinates describing n-fold shape perturbations within each period, and their time derivatives, $\dot{a}_n(t)$, act as velocities or momenta. Unfortunately, truncating the Taylor series results in a poor description of strongly nonlinear dynamics because the conformal map begins to vary wildly near the unit circle.

An alternate approach used by Yoshikawa and Balk [17] is to expand in terms resembling Saffman–Taylor fingers,

$$g(w, t) = \log w + b(t) - \sum_{n=1}^{N} b_n(t) \log(1 - \lambda_n(t) w), \tag{14}$$

which can be viewed as a re-summation of the Taylor series in Eq. (13). As shown in Fig. 3, exact solutions exist with only a finite number of terms in the finger expansion, as long as the new generalized coordinates, $\lambda_n(t)$, stay inside the unit disk, $|\lambda_n| < 1$. This example illustrates the importance of the choice of *shape functions* in the expansion of the conformal map, e.g., w^n vs. $\log(1 - \lambda_n w)$.

2.1.3. Void electro-migration in metals

Micron-scale interconnects in modern integrated circuits, typically made of aluminum, sustain enormous currents and high temperatures. The intense electron wind drives solid-state mass diffusion, especially along dislocations and grain boundaries, where voids also nucleate and grow. In the narrowest and most fragile interconnects, grain boundaries are often well separated enough that isolated voids migrate in a fairly homogeneous environment due to surface diffusion, driven by the electron wind. Voids tend to deform into slits, which propagate across the interconnect, causing it to sever. A theory of void electro-migration is thus important for predicting reliability.

In the simplest two-dimensional model [18], a cylindrical void is modeled as a deformable, insulating inclusion in a conducting matrix. Outside the void,

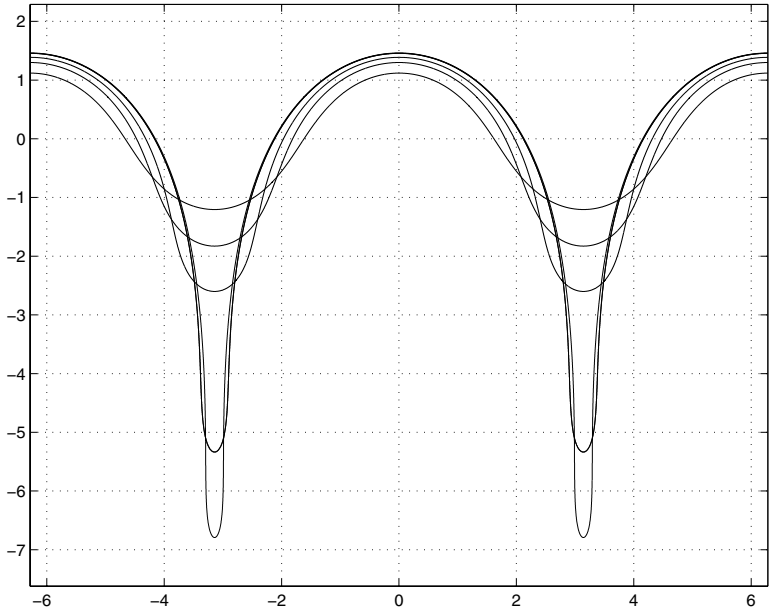

Figure 3. Conformal-map dynamics for the strongly nonlinear regime of the Richtmyer-Meshkov instability [17]. (Courtesy of Toshio Yoshikawa and Alexander Balk.)

the electrostatic potential, ϕ, satisfies Laplace's equation, which invites the use of conformal mapping. The electric field, $\mathbf{E} = -\nabla\phi$, is taken to be uniform far away and wraps around the void surface, due to a Neumann boundary condition, $\hat{\boldsymbol{n}} \cdot \mathbf{E} = 0$.

The difference with Laplacian growth lies in the kinematic condition, which is considerably more complicated. In place of Eq. (6), the normal velocity of the void surface is given by the surface divergence of the surface current, j, which takes the dimensionless form,

$$\hat{\boldsymbol{n}} \cdot \mathbf{v} = \frac{\partial j}{\partial s} = \chi \frac{\partial^2 \phi}{\partial s^2} + \frac{\partial^2 \kappa}{\partial s^2}, \tag{15}$$

where s is the local arc-length coordinate and χ is a dimensionless parameter comparing surface currents due to the electron wind force (first term) and due to gradients in surface tension (second term). This moving free boundary problem somewhat resembles the viscous fingering problem with surface tension, and it admits analogous finger solutions, albeit of width $2/3$, not $1/2$ [19].

To describe the evolution of a singly connected void, we consider the conformal map, $z = g(w, t)$, from the exterior of the unit circle to the exterior of

the void. As long as the map remains univalent, it has a *Laurent series* of the form,

$$g(w,t) = A_1(t)w + A_0(t) + \sum_{n=1}^{\infty} A_{-n}(t)w^{-n}, \quad \text{for } |w| > 1, \tag{16}$$

where the Laurent coefficients, $A_n(t)$, are now the generalized coordinates. As in the case of viscous fingering [3], a hierarchy of nonlinear ordinary differential equations (ODEs) for these coordinates can be derived. For void electromigration, Wang *et al.* [18] start from a variational principle accounting for surface tension and surface diffusion, using a Galerkin procedure. They truncate the expansion after 17 coefficients, so their numerical method breaks down if the void deforms significantly, e.g., into a curved slit. Nevertheless, as shown in Fig. 4(a), the numerical method is able to capture essential features of the early stages of strongly nonlinear dynamics.

In the same regime, it is also possible to incorporate anisotropic surface tension or surface mobility. The latter involves multiplying the surface current by a factor $(1 + g_d \cos m\alpha)$, where α is the surface orientation in the physical z-plane, given at $z = g(e^{i\theta}, t)$, by

$$\alpha = \theta + \arg \frac{\partial g}{\partial w}(e^{i\theta}, t). \tag{17}$$

Some results are shown in Fig. 4(b), where the void develops dynamical facets.

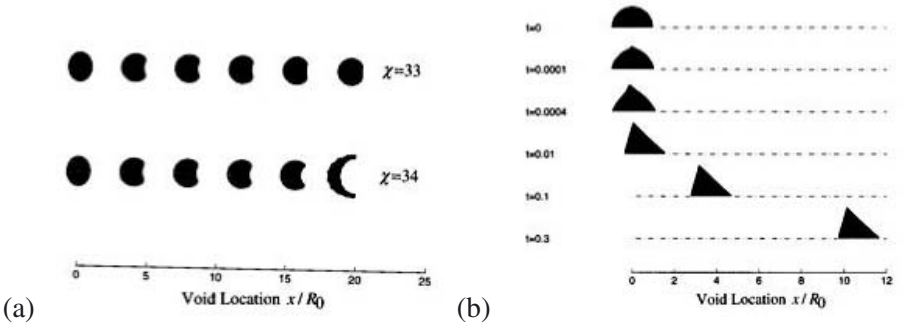

(a) (b)

Figure 4. Numerical conformal-mapping simulations of the electromigration of voids in aluminum interconnects [18]. (a) A small shape perturbation of a cylindrical void decaying (above) or deforming into a curved slit (below), depending on a dimensionless group, χ, comparing the electron wind to surface-tension gradients. (b) A void evolving with anisotropic surface diffusivity ($\chi = 100$, $g_d = 100$, $m = 3$). (Courtesy of Zhigang Suo.)

2.1.4. Quadrature domains

We end this section by commenting on some of the mathematics underlying the existence of exact solutions to continuous-time Laplacian-growth problems. Significantly, much of this mathematics carries over to problems in which the governing field equation is not necessarily harmonic, as will be seen in the following section.

The steadily-translating finger solution (11) of Saffman and Taylor turns out to be but one of an increasingly large number of known exact solutions to the standard Hele–Shaw problem. Saffman [20] himself identified a class of unsteady finger-like solutions. This solution was later generalized by Howison [21] to solutions involving multiple fingers exhibiting such phenomena as *tip-splitting* where a single finger splits into two (or more) fingers. It is even possible to find exact solutions to the more realistic case where there is a second interface further down the channel [22] which must always be the case in any experiment.

Besides finger-like solutions which are characterized by time-evolving conformal mappings having logarithmic branch-point singularities, other exact solutions, where the conformal mappings are rational functions with time-evolving poles and zeros, were first identified by Polubarinova–Kochina and Galin in 1945. Richardson [23] later rediscovered the latter solutions while simultaneously presenting important new theoretical connections between the Hele–Shaw problem and a class of planar domains known as *quadrature domains*. The simplest example of a quadrature domain is a circular disc D of radius r centered at the origin which satisfies the identity

$$\int\int_D h(z)\,\mathrm{d}x\,\mathrm{d}y = \pi r^2 h(0), \tag{18}$$

where $h(z)$ is any function analytic in the disc (and integrable over it). Equation (18), which is known as a *quadrature identity* since it holds for any analytic function $h(z)$, is simply a statement of the well-known *mean-value theorem* of complex analysis [24]. A more general domain D, satisfying a generalized quadrature identity of the form

$$\int\int_D h(z)\,\mathrm{d}x\,\mathrm{d}y = \sum_{k=1}^{N}\sum_{j=0}^{n_k-1} c_{jk} h^{(j)}(z_k) \tag{19}$$

is known as a quadrature domain. Here, $\{z_k \in \mathbb{C}\}$ is a set of points inside D and $h^{(j)}(z)$ denotes the jth derivative of $h(z)$. If one makes the choice $h(z) = z^n$ in (19) the resulting integral quantities have become known as the *Richardson moments* of the domain. Richardson showed that the dynamics of the Hele–Shaw problem is such as to *preserve* quadrature domains. That is, if the initial fluid domain in a Hele–Shaw cell is a quadrature domain at time

$t = 0$, it remains a quadrature domain at later times (so long as the solution does not break down). This result is highly significant and provides a link with many other areas of mathematics including potential theory, the notion of balayage, algebraic curves, Schwarz functions and Cauchy transforms. Richardson [25] discusses many of these connections while Varchenko and Etingof [26] provide a more general overview of the various mathematical implications of Richardson's result. Shapiro [27] gives more general background on quadrature domain theory.

It is a well-known result in the theory of quadrature domains [27] that simply-connected quadrature domains can be parameterized by rational function conformal mappings from a unit circle. Given Richardson's result on the preservation of quadrature domains, this explains why Polubarinova–Kochina and Galin were able to find time-evolving rational function conformal mapping solutions to the Hele–Shaw problem. It also underlies the pole dynamics results of Bensimon and Shraiman [9]. But Richardson's result is not restricted to simply-connected domains; *multiply-connected* quadrature domains are also preserved by the dynamics. Physically this corresponds to time-evolving fluid domains containing multiple bubbles of air. Indeed, motivated by such matters, recent research has focused on the analytical construction of multiply-connected quadrature domains using conformal mapping ideas [28, 29]. In the higher-connected case, the conformal mappings are no longer simply rational functions but are given by conformal maps that are *automorphic functions* (or, meromorphic functions on compact Riemann surfaces). The important point here is that understanding the physical problem from the more general perspective of quadrature domain theory has led the way to the unveiling of more sophisticated classes of exact conformal mapping solutions.

2.2. Bi-Harmonic Fields

Although not as well known as conformal mapping involving harmonic functions, there is also a substantial literature on complex-variable methods to solve the *bi-harmonic equation*,

$$\nabla^2 \nabla^2 \psi = 0, \tag{20}$$

which arises in two-dimensional elasticity [30] and fluid mechanics [31]. Unlike harmonic functions, which can be expressed in terms of a single analytic function (the complex potential), bi-harmonic functions can be expressed in terms of two analytic functions, $f(z)$ and $g(z)$, in *Goursat form* [24]:

$$\psi(z, \bar{z}) = \mathrm{Im}\,[\bar{z} f(z) + g(z)] \tag{21}$$

Note that ψ is no longer just the imaginary part of an analytic function $g(z)$ but also contains the imaginary part of the non-analytic component $\bar{z} f(z)$.

A difficulty with bi-harmonic problems is that the typical boundary conditions (see below) are not conformally invariant, so conformal mapping does not usually generate new solutions by simply a change of variables, as in Eq. (4). Nevertheless, the Goursat form of the solution, Eq. (21), is a major simplification, which enables analytical progress.

2.1.5. Viscous sintering

Sintering describes a process by which a granular compact of particles (e.g., metal or glass) is raised to a sufficiently large temperature that the individual particles become mobile and release surface energy in such a way as to produce inter-particulate bonds. At the start of a sinter process, any two particles which are initially touching develop a thin "neck" which, as time evolves, grows in size to form a more developed bond. In compacts in which the packing is such that particles have more than one touching neighbor, as the necks grow in size, the sinter body densifies and any enclosed pores between particles tend to close up. The macroscopic material properties of the compact at the end of the sinter process depend heavily on the degree of densification. In industrial application, it is crucial to be able to obtain accurate and reliable estimates of the time taken for pores to close (or reduce to a sufficiently small size) within any given initial sinter body in order that industrial sinter times are optimized without compromising the macroscopic properties of the final densified sinter body.

The fluid is modeled as a region $D(t)$ of very viscous, incompressible fluid, in which the velocity field,

$$\mathbf{u} = (u, v) = (\psi_y, -\psi_x) \tag{22}$$

is given by the curl of an out-of-plane vector, whose magnitude is a stream function, $\psi(x, y, t)$, which satisfies the bi-harmonic equation [31]. On the boundary $\partial D(t)$, the tangential stress must vanish and the normal stress must be balanced by the uniform surface tension effect, i.e.,

$$-pn_i + 2\mu e_{ij} = T\kappa n_i, \tag{23}$$

where p is the fluid pressure, μ is the viscosity, T is the surface tension parameter, κ is the boundary curvature, n_i denotes components of the outward normal $\mathbf{n}$ to $\partial D(t)$ and e_{ij} is the usual fluid rate-of-strain tensor. The boundary is time-evolved in a quasi-steady fashion with a normal velocity, V_n, determined by the same kinematic condition, $V_n = \mathbf{u} \cdot \mathbf{n}$, as in viscous fingering.

In terms of the Goursat functions in (21) – which are now generally time-evolving – the stress condition (23) takes the form

$$f(z, t) + z\overline{f'}(\bar{z}, t) + \overline{g'}(\bar{z}, t) = -\frac{i}{2} z_s, \tag{24}$$

Figure 5. Evolution of the solution of Hopper [32] for the coalescence of two equal blobs of fluid under the effects of surface tension.

where again s denotes arc length. Once $f(z,t)$ has been determined from (24), the kinematic condition

$$\mathrm{Im}[z_t \bar{z}_s] = \mathrm{Im}[-2f(z,t)\bar{z}_s] - \tfrac{1}{2} \tag{25}$$

is used to time-advance the interface.

A significant contribution was made by Hopper [32] who showed, using complex variable methods based on the decomposition (21), that the problem for the surface-tension driven coalescence of two equal circular blobs of viscous fluid can be reduced to the evolution of a rational function conformal map, from a unit w-circle, of the form

$$g(w,t) = \frac{R(t)w}{w^2 - a^2(t)}. \tag{26}$$

The two time-evolving parameters $R(t)$ and $a(t)$ satisfy two coupled nonlinear ODEs. Figure 5 shows a sequence of shapes of the two coalescing blobs computed using Hopper's solution. At large times, the configuration equilibrates to a single circular blob.

While Hopper's coalescence problem provides insight into the growth of the inter-particle neck region, there are no pores in this configuration and it is natural to ask whether more general exact solutions exist. Crowdy [33] reappraised the viscous sintering problem and showed, in direct analogy with Richardson's result on Hele–Shaw flows, that the dynamics of the sintering problem is also such as to preserve quadrature domains. As in the Hele–Shaw problem, this perspective paved the way for the identification of new exact solutions, generalizing (26), for the evolution of doubly-connected fluid regions. Figure 6 shows the shrinkage of a pore enclosed by a typical "unit" in a doubly-connected square packing of touching near-circular blobs of viscous fluid. This calculation employs a conformal mapping to the doubly-connected fluid region (which is no longer a rational function but a more general automorphic function) derived by Crowdy [34] and, in the same spirit as Hopper's solution (26), requires only the integration of three coupled nonlinear ODEs. The fluid regions shown in Fig. 6 are all doubly-connected quadrature domains. Richardson [35] has also considered similar Stokes flow problems using a different conformal mapping approach.

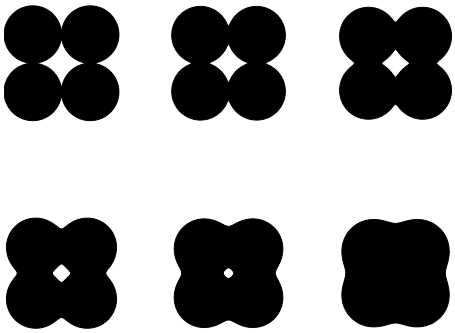

Figure 6. The coalescence of fluid blobs and collapse of cylindrical pores in a model of viscous sintering. This sequence of images shows an analytical solution by Crowdy [34] using complex-variable methods.

2.1.6. Pores in elastic solids

Solid elasticity in two dimensions is also governed by a bi-harmonic function, the Airy stress function [30]. Therefore, the stress tensor, σ_{ij}, and the displacement field, u_i, may be expressed in terms of two analytic functions, $f(z)$ and $g(z)$:

$$\frac{\sigma_{22}+\sigma_{11}}{2} = f'(z) + \overline{f'}(\overline{z}) \tag{27}$$

$$\frac{\sigma_{22}-\sigma_{11}}{2} + i\sigma_{12} = \overline{z}\, f''(z) + g'(z) \tag{28}$$

$$\frac{Y}{1+\nu}(u_1 + iu_2) = \kappa f(z) - z\overline{f'}(\overline{z}) - \overline{g}(\overline{z}) \tag{29}$$

where Y is Young's modulus, ν is Poisson's ratio, and $\kappa = (3-\nu)/(1+\nu)$ for plane stress and $\kappa = 3-4\nu$ for plane strain. As with bubbles in viscous flow, the use of Goursat functions allows conformal mapping to be applied to bi-harmonic free boundary problems in elastic solids, without solving explicitly for bulk stresses and strains.

For example, Wang and Suo [36] have simulated the dynamics of a singly-connected pore by surface diffusion in an infinite stressed elastic solid. As in the case of void electromigration described above, they solve nonlinear ODEs for the Laurent coefficients of the conformal map from the exterior of the unit disk, Eq. (16). Under uniaxial tension, there is a competition between surface tension, which prefers a circular shape, and the applied stress, which drives elongation and eventually fracture in the transverse direction. The numerical method, based on the truncated Laurent expansion, is able to capture the transition from stable elliptical shapes at small applied stress to the unstable growth

of transverse protrusions at large applied stress, although naturally it breaks down when cusps resembling crack tips begin to form.

2.3. Non-Harmonic Conformally Invariant Fields

The vast majority of applications of conformal mapping fall into one of the two classes above, involving harmonic or bi-harmonic functions, where the connections with analytic functions, Eqs. (4) and (21), are cleverly exploited. It turns out, however, that conformal mapping can be applied just as easily to a broad class of problems involving non-harmonic fields, recently discovered by Bazant [37]. Of course, in planar geometry, the conformal map itself is described by an analytic function, but the fields need not be, as long as they transform in a simple way under conformal mapping.

The most convenient fields satisfy *conformally invariant* partial differential equations (PDEs), whose forms are unaltered by a conformal change of variables. It is straightforward to transform PDEs under a conformal mapping of the plane, $w = f(z)$, by expressing them in terms of complex gradient operator introduced above,

$$\nabla_z = \frac{\partial}{\partial x} + i\frac{\partial}{\partial y} = 2\frac{\partial}{\partial \overline{z}}, \tag{30}$$

which we have related to the $\overline{z}$ partial derivative using the Cauchy–Riemann equations, Eq. (1). In this form, it is clear that $\nabla_z f = 0$ if and only if $f(z)$ is analytic, in which case $\overline{\nabla}_z f = 2f'$. Using the chain rule, also obtain the transformation rule for the gradient,

$$\nabla_z = \overline{f'}\,\nabla_w. \tag{31}$$

To apply this formalism, we write Laplace's equation in the form,

$$\mathbf{\nabla}_z^2 \phi = \mathrm{Re}\,\nabla_z \overline{\nabla}_z \phi = \nabla_z \overline{\nabla}_z \phi = 0, \tag{32}$$

which assumes that mixed partial derivatives can be taken in either order. (Note that $\mathbf{a}\cdot\mathbf{b} = \mathrm{Re}\,a\overline{b}$.) The conformal invariance of Laplace's equation, $\nabla_w \overline{\nabla}_w \phi = 0$, then follows from a simple calculation,

$$\nabla_z \overline{\nabla}_z = (\nabla_z f')\overline{\nabla}_w + |f'|^2 \nabla_w \overline{\nabla}_w = |f'|^2\,\nabla_w \overline{\nabla}_w, \tag{33}$$

where $\nabla_z f' = 0$ because f' is also analytic. As a result of conformal invariance, any harmonic function in the w-plane, $\phi(w)$, remains harmonic in the z-plane, $\phi(f(z))$, after the simple substitution, $w = f(z)$. We came to the same conclusion above in Eq. (4), using the connection between harmonic and analytic functions, but the argument here is more general and also applies to other PDEs.

The bi-harmonic equation is not conformally invariant, but some other equations – and systems of equations – are. The key observation is that any "product of two gradients" transforms in the same way under conformal mapping, not only the Laplacian, $\boldsymbol{\nabla} \cdot \boldsymbol{\nabla}\phi$, but also the term, $\boldsymbol{\nabla}\phi_1 \cdot \boldsymbol{\nabla}\phi_2 = \mathrm{Re}(\nabla\phi_1)\overline{\nabla}\phi_2$, which involves *two* real functions, ϕ_1 and ϕ_2:

$$\mathrm{Re}(\nabla_z\phi_1)\,\overline{\nabla}_z\phi_2 = |f'|^2\,\mathrm{Re}(\nabla_w\phi_1)\,\overline{\nabla}_w\phi_2. \tag{34}$$

(Todd Squires has since noted that the operator, $\boldsymbol{\nabla}\phi_1 \times \boldsymbol{\nabla}\phi_2 = \mathrm{Im}(\nabla\phi_1)\overline{\nabla\phi_2}$, also transforms in the same way.) These observations imply the conformal invariance of a broad class of systems of nonlinear PDEs:

$$\sum_{i=1}^{N}\left(a_i\,\boldsymbol{\nabla}^2\phi_i + \sum_{j=i}^{N} a_{ij}\,\boldsymbol{\nabla}\phi_i\cdot\boldsymbol{\nabla}\phi_j \;+\; \sum_{j=i+1}^{N} b_{ij}\,\boldsymbol{\nabla}\phi_i\times\boldsymbol{\nabla}\phi_j\right) = 0, \tag{35}$$

where the coefficients $a_i(\phi)$, $a_{ij}(\phi)$, and $b_{ij}(\phi)$ may be nonlinear functions of the unknowns, $\phi = (\phi_1, \phi_2, \ldots, \phi_N)$, but not of the independent variables or any derivatives of the unknowns.

The general solutions to these equations are not harmonic and thus depend on both z and $\overline{z}$. Nevertheless, conformal mapping works in precisely the same way: A solution, $\phi(w, \overline{w})$, can be mapped to another solution, $\phi(f(z), \overline{f(z)})$, by a simple substitution, $w = f(z)$. This allows the conformal mapping techniques above (and below) to be extended to new kinds of moving free boundary problems.

2.1.7. Transport-limited growth phenomena

For physical applications, the conformally invariant class, Eq. (35), includes the important set of steady conservation laws for gradient-driven flux densities,

$$\frac{\partial c_i}{\partial t} = \boldsymbol{\nabla}\cdot\mathbf{F}_i = 0, \qquad \mathbf{F}_i = c_i\,\mathbf{u}_i - D_i(c_i)\,\boldsymbol{\nabla}c_i, \quad \mathbf{u}_i \propto \boldsymbol{\nabla}\phi, \tag{36}$$

where $\{c_i\}$ are scalar fields, such as chemical concentrations or temperature, $\{D_i(c_i)\}$ are nonlinear diffusivities, $\{\mathbf{u}_i\}$ are irrotational vector fields causing advection, and ϕ is a potential [37]. Physical examples include advection-diffusion, where ϕ is the harmonic velocity potential, and electrochemical transport, where ϕ is the non-harmonic electrostatic potential, determined implicitly by electro-neutrality.

By modifying the classical methods described above for Laplacian growth, conformal-map dynamics can thus be formulated for more general, transport-limited growth phenomena [38]. The natural generalization of the kinematic condition, Eq. (6), is that the free boundary moves in proportion to one of

the gradient-driven fluxes with velocity, $\mathbf{v} \propto \mathbf{F}_1$. For the growth of a finite filament, driven by prescribed fluxes and/or concentrations at infinity, one obtains a generalization of the Polubarinova–Galin equation for the conformal map, $z = g(w, t)$, from the exterior of the unit disk to the exterior of growing object,

$$\mathrm{Re}(\overline{w\, g'}\, g_t) = \sigma(w, t) \quad \text{on } |w| = 1, \tag{37}$$

where $\sigma(w, t)$ is the non-constant, time-dependent normal flux, $\hat{n} \cdot \mathbf{F}_1$, on the unit circle in the mathematical plane.

2.1.8. *Solidification in a fluid flow*

A special case of the conformally invariant Eq. (35) has been known for almost a century: steady advection-diffusion of a scalar field, c, in a potential flow, $\mathbf{u}$. The dimensionless PDEs are

$$\mathrm{Pe}\, \mathbf{u} \cdot \boldsymbol{\nabla} c = \boldsymbol{\nabla}^2 c, \quad \mathbf{u} = \boldsymbol{\nabla}\phi, \quad \boldsymbol{\nabla}^2 \phi = 0, \tag{38}$$

where we have introduced the Péclet number, $\mathrm{Pe} = UL/D$, in terms of a characteristic length, L, velocity, U, and diffusivity, D. In 1905, Boussinesq showed that Eq. (38) takes a simpler form in *streamline coordinates*, (ϕ, ψ), where $\Phi = \phi + i\,\psi$ is the complex velocity potential:

$$\mathrm{Pe}\, \frac{\partial c}{\partial \phi} = \left(\frac{\partial^2 c}{\partial \phi^2} + \frac{\partial^2 c}{\partial \psi^2} \right) \tag{39}$$

because advection (the left hand side) is directed only along streamlines, while diffusion (the right hand side) also occurs in the transverse direction, along isopotential lines. From the general perspective above, we recognize this as the conformal mapping of an invariant system of PDEs of the form (36) to the complex Φ plane, where the flow is uniform and any obstacles in the flow are mapped to horizontal slits.

Streamline coordinates form the basis for Maksimov's method for interfacial growth by steady advection-diffusion in a background potential flow, which has been applied to freezing in ground-water flow and vapor deposition on textile fibers [4, 39]. The growing interface is a streamline held at a fixed concentration (or temperature) relative to the flowing bulk fluid at infinity. This is arguably the simplest growth model with two competing transport processes, and yet open questions remain about the nonlinear dynamics, even without surface tension.

The normal flux distribution to a finite absorber in a uniform background flow, $\sigma(w, t)$ in Eq. (37) is well known, but rather complicated [40], so it is replaced by asymptotic approximations for analytical work, such as

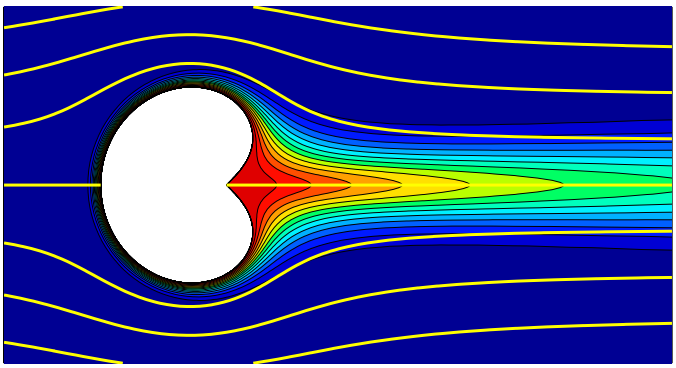

Figure 7. The exact self-similar solution, Eq. (40), for continuous advection-diffusion-limited growth in a uniform background potential flow (yellow streamlines) at the dynamical fixed point (Pe = ∞). The concentration field (color contour plot) is shown for Pe = 100. (Courtesy of Jaehyuk Choi.)

$\sigma \sim 2\sqrt{\mathrm{Pe}/\pi}\,\sin(\theta/2)$ as $\mathrm{Pe} \to \infty$, which is the fixed point of the dynamics. In this important limit, Choi *et al.* [41] have found an exact similarity solution,

$$g(w,t) = A_1(t)\sqrt{w(w-1)}, \qquad A_1(t) = t^{2/3} \tag{40}$$

to Eq. (37) with $\sigma(e^{i\theta},t) = \sqrt{A_1(t)}\,\sin(\theta/2)$ (since $\mathrm{Pe}(t) \propto A_1(t)$ for a fixed background flow). As shown in Fig. 7, this corresponds to a constant shape, whose linear size grows like $t^{2/3}$, with a 90° cusp at the rear stagnation point, where a branch point of $\sqrt{w(w-1)}$ lies on the unit circle. For any finite, $\mathrm{Pe}(t)$, however, the cusp is smoothed, and the map remains univalent, although other singularities may form. Curiously, when mapped to the channel geometry with $\log z$, the solution (40) becomes a Saffman–Taylor finger of width, $\lambda = 3/4$.

3. Stochastic Interfacial Dynamics

The continuous dynamics of conformal maps is a mature subject, but much attention is now focusing on analogous problems with discrete, stochastic dynamics. The essential change is in the kinematic condition: The expression for the interfacial velocity, e.g., Eq. (6), is re-interpreted as the probability density (per unit arc length) for advancing the interface with a discrete "bump", e.g., to model a depositing particle. Continuous conformal-map dynamics is then replaced by rules for constructing and composing the bumps. This method of *iterated conformal maps* was introduced by Hastings and Levitov [42] in the context of Laplacian growth.

Stochastic Laplacian growth has been discussed since the early 1980s, but Hastings and Levitov [42] first showed how to implement it with conformal mapping. They proposed the following family of *bump functions*,

$$f_{\lambda,\theta}(w) = e^{i\theta} f_\lambda \left(e^{-i\theta} w \right), \quad |w| \geq 1 \tag{41}$$

$$f_\lambda(w) = w^{1-a} \left[\frac{(1+\lambda)(w+1)}{2w} \left(w+1+\sqrt{w^2+1-2w\frac{1-\lambda}{1+\lambda}} \right) -1 \right]^a \tag{42}$$

as elementary univalent mappings of the exterior of the unit disk used to advance the interface ($0 < a \leq 1$). The function, $f_{\lambda,\theta}(w)$, places a bump of (approximate) area, λ, on the unit circle, centered at angle, θ. Compared to analytic functions of the unit disk, the Hastings–Levitov function (42) generates a much more localized perturbation, focused on the region between two branch points, leaving the rest of the unit circle unaltered [43]. For $a = 1$, the map produces a *strike*, which is a line segment of length $\sqrt{\lambda}$ emanating normal to the circle. For $a = 1/2$, the map is an invertible composition of simple linear, Möbius and Joukowski transformations, which inserts a semi-circular *bump* on the unit circle. As shown in Fig. 8, this yields a good description of aggregating particles, although other choices, like $a = 2/3$, have also been considered [43]. Quantifying the effect of the bump shape remains a basic open question.

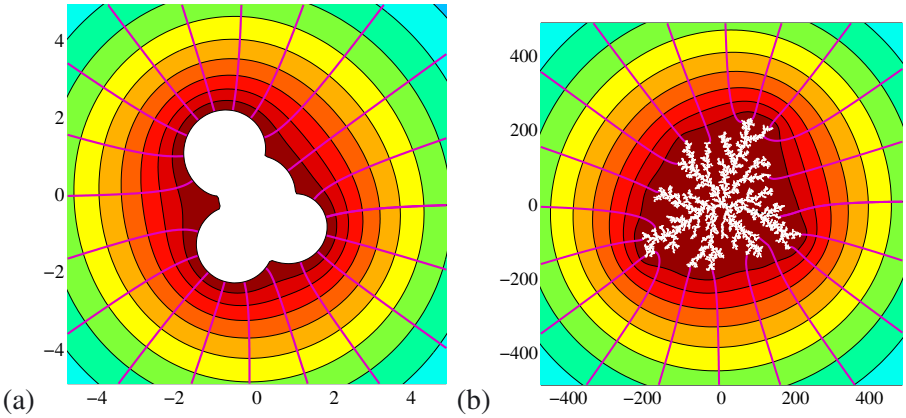

Figure 8. Simulation of the aggregation of (a) 4 and (b) 10 000 particles using the Hastings–Levitov algorithm ($a = 1/2$). Color contours show the quasi-steady concentration (or probability) field for mobile particles arriving from infinity, and purple curves indicate lines of diffusive flux (or probability current). (Courtesy of Jaehyuk Choi and Benny Davidovitch.)

Once the bump function is chosen, the conformal map, $z = g_n(w)$, from the exterior of the unit disk to the evolving domain with n bumps is constructed by iteration,

$$g_n(w) = g_{n-1}\left(f_{\lambda_n,\theta_n}(w)\right) \tag{43}$$

starting from the initial interface, given by $g_0(w)$. All of the physics is contained in the sequence of bump parameters, $\{(\lambda_n, \theta_n)\}$, which can be generated in different ways (in the w plane) to model a variety of physical processes (in the z-plane). As shown in Fig. 8(b), the interface often develops a very complicated, fractal structure, which is given, quite remarkably, by an exact mapping of the unit circle.

The great advantage of stochastic conformal mapping over atomistic or Monte Carlo simulation of interfacial growth lies in its mathematical insight. For example, given the sequence $\{(\lambda_n, \theta_n)\}$ from a simulation of some physical growth process, the Laurent coefficients, $A_k(n)$, of the conformal map, $g_n(w)$, as defined in Eq. (16), can be calculated analytically. For the bump function (42), Davidovitch *et al.* [43] provide a hierarchy of recursion relations, yielding formulae such as

$$A_1(n) = \prod_{m=1}^{n} (1 + \lambda_m)^a, \tag{44}$$

and explain how to interpret the Laurent coefficients. For example, A_1 is the *conformal radius* of the cluster, a convenient measure of its linear extent. It is also the radius of a grounded disk with the same capacitance (with respect to infinity) as the cluster. The Koebe "1/4 theorem" on univalent functions [44] ensures that the cluster (image of the unit disk) is always contained in a disk of radius $4A_1$. The next Laurent coefficient, A_0, is the center of a uniformly charged disk, which would have the same asymptotic electric field as the cluster (if also charged). Similarly, higher Laurent coefficients encode higher multipole moments of the cluster.

Mapping the unit circle with a truncated Laurent expansion defines the *web*, which wraps around the growing tips and exhibits a sort of turbulent dynamics, endlessly forming and smoothing cusp-like protrusions [42, 45]. The stochastic dynamics, however, does not suffer from finite-time singularities because the iterated map, by construction, remains univalent. In some sense, discreteness plays the role of surface tension, as another regularization of ill-posed continuum models like Laplacian growth.

3.1. Diffusion-Limited Aggregation (DLA)

The stochastic analog of Laplacian growth is the DLA model of Witten and Sander [46], illustrated in Fig. 8, in which particles perform random walks

one-by-one from infinity until they stick irreversibly to a cluster, which grows from a seed at the origin. DLA and its variants (see below) provide simple models for many fractal patterns in nature, such as colloidal aggregates, dendritic electro-deposits, snowflakes, lightning strikes, mineral deposits, and surface patterns in ion-beam microscopy [14]. In spite of decades of research, however, DLA still presents theoretical mysteries, which are just beginning to unravel [47].

The Hastings–Levitov algorithm for DLA prescribes the bump parameters, $\{(\lambda_n, \theta_n)\}$, as follows. As in Laplacian growth, the harmonic function for the concentration (or probability density) of the next random walker approaching an n-particle cluster is simply,

$$\phi_n(z) = A \,\mathrm{Re}\, \log g_n^{-1}(z), \tag{45}$$

according to Eq. (4), since $\phi(w) = A \,\mathrm{Re}\, \log w = A \log|w|$ is the (trivial) solution to Laplace's equation in the mathematical w plane with $\phi = 0$ on the unit disk with a circularly symmetric flux density, A, prescribed at infinity. Using the transformation rule, Eq. (31), we then find that the evolving *harmonic measure*, $p_n(z)|\mathrm{d}z|$, for the nth growth event corresponds to a uniform probability measure, $P_n(\theta)\,\mathrm{d}\theta$, for angles, θ_n, on the unit circle, $w = e^{i\theta}$:

$$p_n(z)|\mathrm{d}z| = |\nabla_z \phi||\mathrm{d}z| = \left|\frac{\nabla_w \phi}{g'_{n-1}}\right| |g'_{n-1}\,\mathrm{d}w| = |\nabla_w \phi||\mathrm{d}w| = \frac{\mathrm{d}\theta}{2\pi} = P_n(\theta)\,\mathrm{d}\theta, \tag{46}$$

where we set $A = 1/2\pi$ for normalization, which implicitly sets the time scale. The conformal invariance of the harmonic measure is well known in mathematics, but the surprising result of Hastings and Levitov [42] is that all the complexity of DLA is slaved to a sequence of independent, uniform random variables.

Where the complexity resides is in the bump area, λ_n, which depends non-trivially on current cluster geometry and thus on the entire history of random angles, $\{\theta_m \,|\, m \le n\}$. For DLA, the bump area in the mathematical w plane should be chosen such that it has a fixed value, λ_0, in the physical z-plane, equal to the aggregating particle area. As long as the new bump is sufficiently small, it is natural to try to correct only for the Jacobian factor

$$J_n(w) = |g'_n(w)|^2 \tag{47}$$

of the previous conformal map at the center of the new bump,

$$\lambda_n = \frac{\lambda_0}{J_{n-1}(e^{i\theta_n})}, \tag{48}$$

although it is not clear *a priori* that such a local approximation is valid. Note at least that $g_n' \to \infty$, and thus $\lambda_n \to 0$, as the cluster grows, so this has a chance of working.

Numerical simulations with the Hastings–Levitov algorithm do indeed produce nearly constant bump areas, as in Fig. 8. Nevertheless, much larger "particles", which fill deep fjords in the cluster, occasionally occur where the map varies too wildly, as shown in Fig. 9(a). It is possible (but somewhat

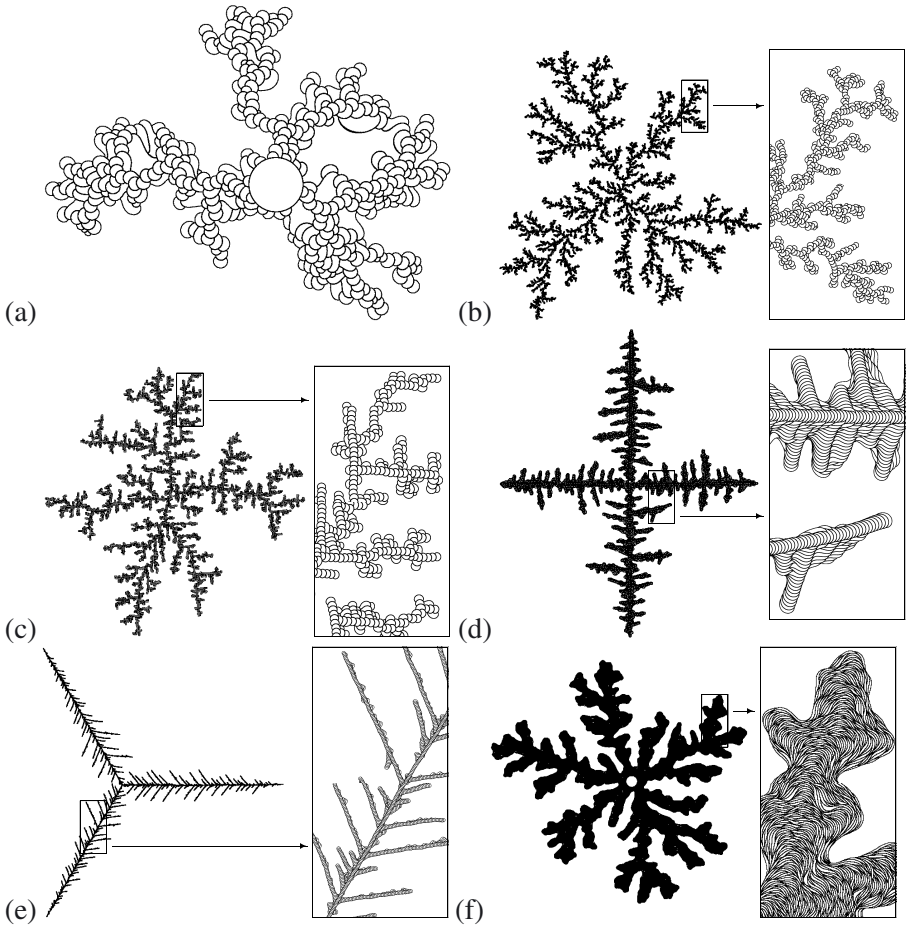

Figure 9. Simulations of fractal aggregates by Stepanov and Levitov [48]: (a) Superimposed time series of the boundary, showing the aggregation of particles, represented by iterated conformal maps; (b) a larger simulation with a particle-area acceptance window; (c) the result of anisotropic growth probability with square symmetry; (d) square-anisotropic growth with noise control via flat particles; (e) triangular-anisotropic growth with noise control; (f) isotropic growth with noise control, which resembles radial viscous fingering. (Courtesy of Leonid Levitov.)

unsatisfying) to reject particles outside an "area acceptance window" to produce rather realistic DLA clusters, as shown in Fig. 9(b). It seems that the rejected large bumps are so rare that they do not much influence statistical scaling properties of the clusters [48], although this issue is by no means rigorously resolved.

3.2. Fractal Geometry

Fractal patterns abound in nature, and DLA provides the most common way to understand them [14]. The fractal scaling of DLA has been debated for decades, but conformal dynamics is shedding new light on the problem. Simulations show that the conformal radius (44) exhibits fractal scaling, $A_1(n) \propto n^{1/D_f}$, where the *fractal dimension*, $D_f = 1.71$, agrees with the accepted value from Monte Carlo (random walk) simulations of DLA, although the prefactor seems to depend on the bump function [43]. A perturbative renormalization-group analysis of the conformal dynamics by Hastings [45] gives a similar result, $D_f = 2 - 1/2 + 1/5 = 1.7$. The multifractal spectrum of the harmonic measure has also been studied [49, 50].

Perhaps the most basic question is whether DLA clusters are truly fractal – statistically self-similar and free of any length scale. This long-standing question requires accurate statistics and very large simulations, to erase the surprisingly long memory of the initial conditions. Conformal dynamics provides exact formulae for cluster moments, but simulations are limited to at most 10^5 particles by poor $O(n^2)$ scaling, caused by the history-dependent Jacobian in Eq. (48). In contrast, efficient random-walk simulations can aggregate many millions of particles.

Therefore, Somfai *et al.* [51] developed a hybrid method relying only upon the existence of the conformal map, but not the Hastings–Levitov algorithm to construct it. Large clusters by Monte Carlo simulation, and approximate Laurent coefficients are computed, purely for their morphological information, as follows. For a given cluster of size N, M random walkers are launched from far away, and the positions, z_m, where they would first touch the cluster, are recorded. If the conformal map, $z = g_n(e^{i\theta})$, were known, the points z_m would correspond to M angles θ_m on the unit circle. Since these must sample a uniform distribution, one assumes $\theta_m = 2\pi m/M$ for large M. From Eq. (16), the Laurent coefficients are simply the Fourier coefficients of the discretely sampled function, $z_m = \sum A_k e^{i\theta_m k}$. Using this method, all Laurent coefficients appear to scale with the same fractal dimension,

$$\langle |A_k(n)|^2 \rangle \propto n^{2/D_f} \tag{49}$$

although the first few coefficients crossover extremely slowly to the asymptotic scaling.

3.3. Snowflakes and Viscous Fingers

In conventional Monte Carlo simulations, many variants of DLA have been proposed to model real patterns found in nature [14]. For example, clusters closely resembling snowflakes can be grown by a combination of noise control (requiring multiple hits before attachment) and anisotropy (on a lattice). Conformal dynamics offers the same flexibility, as shown in Fig. 9, while allowing anisotropy and noise to be controlled independently [48]. Anisotropy can be introduced in the growth probability with a weight factor, $1 + c \cos m\alpha_n$, where α_n is the surface orientation angle in the physical plane given by Eq. (17), or by simply rejecting angles outside some tolerance from the desired symmetry directions. Noise can be controlled by flattening the aspect ratio of the bumps. Without anisotropy, this produces smooth fluid-like patterns (Fig. 9(f)), reminiscent of viscous fingers (Fig. 2).

The possible relation between DLA and viscous fingering is a tantalizing open question in pattern formation. Many authors have argued that the regularization of finite-time singularities in Laplacian growth by discreteness is somehow analogous to surface tension. Indeed, the average DLA cluster in a channel, grown by conformal mapping, is similar (but not identical) to a Saffman–Taylor finger of width 1/2 [52], and the instantaneous expected growth rate of a cluster can be related to the Polubarinova–Galin (or "Shraiman–Bensimon") equation [42]. Conformal dynamics with many bumps grown simultaneously suggests that Laplacian growth and DLA are in different universality classes, due to the basic difference of layer-by-layer vs. one-by-one growth, respectively [53]. Another multiple-bump algorithm with complete surface coverage, however, seems to yield the opposite conclusion [54].

3.4. Dielectric Breakdown

In their original paper, Hastings and Levitov [42] allowed for the size of the bump in the physical plane to vary with an exponent, α, by replacing J_{n-1} with $(J_{n-1})^{\alpha/2}$ in Eq. (48). In DLA ($\alpha = 2$), the bump size is roughly constant, but for $0 < \alpha < 2$ the bump size grows with the local gradient of the Laplacian field. This is a simple model for dielectric breakdown, where the stochastic growth of an electric discharge penetrating a material is nonlinearly enhanced by the local electric field. One could use strikes ($a = 0$) rather than bumps ($a = 1/2$) to better reproduce the string-like branched patterns seen in laboratory experiments [14] and more familiar lightning strikes.

The model displays a "stable-to-turbulent" phase transition: The relative surface roughness decreases with time for $0 \leq \alpha < 1$ and grows for $\alpha > 1$.

The original Dielectric Breakdown Model (DBM) of Niemeyer *et al.* [55] has a more complicated conformal-dynamics representation. As usual, the

growth is driven by the gradient of a harmonic function, ϕ (the electrostatic potential) on an iso-potential surface (the discharge region). Unlike the α-model above, however, DBM growth events are assumed to have constant size, so the bump size in the mathematical plane is still chosen according to Eq. (48). The difference lies in the growth measure, which does not obey Eq. (46). Instead, the generalized harmonic measure in the physical z-plane is given by

$$p(z) \propto |\nabla_z \phi|^\eta, \tag{50}$$

where η is an exponent interpolating between the Eden model ($\eta = 0$), DLA ($\eta = 1$), and nonlinear dielectric breakdown ($\eta > 1$). For $\eta \neq 1$, the fortuitous cancellation in Eq. (46) does not occur. Instead, a similar calculation using Eq. (45) yields a non-uniform probability measure for the nth angle on the unit circle in the mathematical plane,

$$P_n(\theta_n) = |g'_{n-1}(e^{i\theta_n})|^{1-\eta}, \tag{51}$$

which is complicated and depends on the entire history of the simulation.

Nevertheless, conformal mapping can be applied fruitfully to DBM, because not solving Laplace's equation around the cluster outweighs the difficulty of sampling the angle measure. Surmounting the latter with a Monte Carlo algorithm, Hastings [56] has performed DBM simulations of 10^4 growth events, an order of magnitude beyond standard methods solving Laplace's equation on a lattice. The results, illustrated in Fig. 10, support the theoretical conjecture that DBM clusters become one-dimensional, and thus non-fractal, for $\eta \geq 4$.

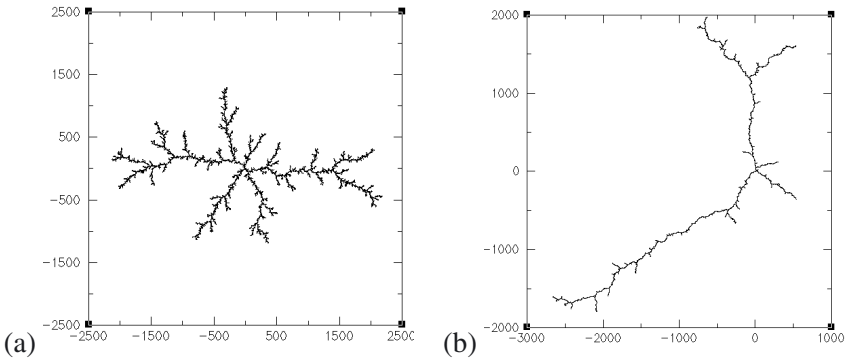

Figure 10. Conformal-mapping simulations by Hastings [56] of the Dielectric Breakdown Model with (a) $\eta = 2$ and (b) $\eta = 3.5$. (Courtesy of Matt Hastings.)

Using the conformal-mapping formalism, efforts are also underway to develop a unified scaling theory of the η-model for the growth probability from DBM combined with the α-model above for the bump size [50].

3.5. Brittle Fracture

Modeling the stochastic dynamics of fracture is a daunting problem, especially in heterogeneous materials [14, 57]. The basic equations and boundary conditions are still the subject of debate, and even the simplest models are difficult to solve. In two dimensions, stochastic conformal mapping provides an elegant, new alternative to discrete-lattice and finite-element models.

In brittle fracture, the bulk material is assumed to obey Lamé's equation of linear elasticity,

$$\rho \frac{\partial^2 \mathbf{u}}{\partial t^2} = (\lambda + \mu)\nabla(\nabla \cdot \mathbf{u}) + \mu \nabla^2 \mathbf{u}, \tag{52}$$

where $\mathbf{u}$ is the displacement field, ρ is the density, and μ and λ are Lamé's constants. For conformal mapping, it is crucial to assume (i) two-dimensional symmetry of the fracture pattern and (ii) quasi-steady elasticity, which sets the left hand side to zero to obtain equations of the type described above. For Mode III fracture, where a constant out-of-plane shear stress is applied at infinity, we have $\nabla \cdot \mathbf{u} = 0$, so the steady Lamé equation reduces to Laplace's equation for the out-of-plane displacement, $\nabla^2 u_z = 0$, which allows the use of complex potentials. For Modes I and II, where a uniaxial, in-plane tensile stress is applied at infinity, the steady Lamé equation must be solved. As discussed above, this is equivalent to the bi-harmonic equation for the Airy stress function, which allows the use of Goursat functions.

For all three modes, the method of iterated conformal maps can be adapted to produce fracture patterns for a variety of physical assumptions about crack dynamics [58]. For Modes I and II fracture, these models provide the first examples of stochastic bi-harmonic growth, which have interesting differences with stochastic Laplacian growth for Mode III fracture. The Hastings–Levitov formalism is used with constant-size bumps, as in DLA, to represent the fracture process zone, where elasticity does not apply. The growth measure a function of the excess tangential stress, beyond a critical yield stress, σ_c, characterizing the local strength of the material. Quenched disorder is easily included by making σ_c a random variable. In spite of its many assumptions, the method provides analytical insights, while obviating the need to solve Eq. (52) during fracture dynamics, so it merits further study.

3.6. Advection-Diffusion-Limited Aggregation

Non-local fractal growth models typically involve a single bulk field driving the dynamics, such as the particle concentration in DLA, the electric field in DBM, or the strain field in brittle fracture, and as a result these models tend to yield statistically similar structures, apart from the effect of boundary conditions. Pattern formation in nature, however, is often fueled by multiple transport processes, such as diffusion, electromigration, and/or advection in a fluid flow. The effect of such dynamical competition on growth morphology is an open question, which would be difficult to address with lattice-based or finite-element methods, since many large fractal clusters must be generated to fully explore the space and time dependence.

Once again, conformal mapping provides a convenient means to formulate stochastic analogs of the non-Laplacian transport-limited growth models from Section 2.3 (in two dimensions). It is straightforward to adapt the Hastings–Levitov algorithm to construct stochastic dynamics driven by bulk fields satisfying the conformally invariant system of Eq. (35). A class of such models has recently been formulated by Bazant *et al.* [38].

Perhaps the simplest case involving two transport processes, illustrated in Fig. 11, is Advection-Diffusion-Limited Aggregation (ADLA), or "DLA in a flow". Imagine a fluid carrying a dilute concentration of sticky particles flowing past a sticky object, which begins to collect a fractal aggregate. As the cluster grows, it causes the fluid to flow around it and changes the concentration field, which in turn alters the growth probability measure. Assuming a quasi-steady potential flow with a uniform speed far from the cluster, the dimensionless transport problem is

$$\mathrm{Pe}_0 \nabla\phi \cdot \nabla c = \nabla^2 c, \quad \nabla^2\phi = 0, \qquad z \in \Omega_z(t), \tag{53}$$

$$c = 0, \quad \hat{\boldsymbol{n}} \cdot \nabla\phi = 0, \quad \sigma = \hat{\boldsymbol{n}} \cdot \nabla c, \qquad z \in \partial\Omega_z(t), \tag{54}$$

$$c \to 1, \quad \nabla\phi \to \hat{\boldsymbol{x}}, \qquad |z| \to \infty, \tag{55}$$

where Pe_0 is the initial Péclet number and σ is the diffusive flux to the surface, which drives the growth. The transport problem is solved in the mathematical w-plane, where it corresponds to a uniform potential flow of concentrated fluid past an absorbing circular cylinder. The normal diffusive flux on the cylinder, $\sigma(\theta, \mathrm{Pe})$, can be obtained from a tabulated numerical solution or an accurate analytical approximation [40].

Because the boundary condition on ϕ at infinity is not conformally invariant, the flow in the w-plane has a time-dependent Péclet number, $\mathrm{Pe}(t) = A_1(t)\mathrm{Pe}_0$, which grows with the conformal radius of the cluster. As a result, the

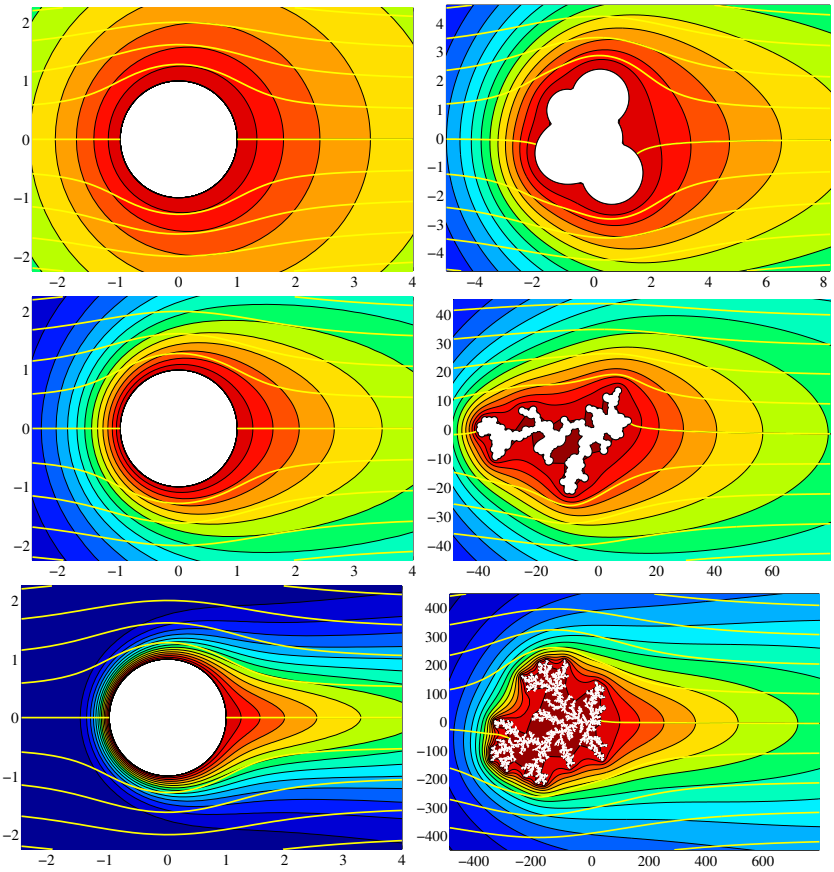

Figure 11. A simulation of Advection-Diffusion-Limited Aggregation from Bazant *et al.* [38] In each row, the growth probabilities in the physical z-plane (on the right) are obtained by solving advection-diffusion in a potential flow past an absorbing cylinder in the mathematical w-plane (on the left), with the same time-dependent Pélcet number.

probability of the nth growth event is given by a time-dependent, non-uniform measure for the angle on the unit circle,

$$P_n(\theta_n) = \frac{\beta}{\lambda_0}\,\tau_n\,\sigma\left(e^{i\theta_n}, A_1(t_{n-1})\right), \tag{56}$$

where β is a constant setting the mean growth rate. The waiting time between growth events is an exponential random variable with mean, τ_n, given by the current integrated flux to the object,

$$\frac{\lambda_0}{\beta\tau_n} = \int_0^{2\pi} \sigma\left(e^{i\theta}, A_1(t_{n-1})\right) \mathrm{d}\theta. \tag{57}$$

Unlike DLA, the aggregation speeds up as the cluster grows, due to a larger cross section to catch new particles in the flow.

As shown in Fig. 11, the model displays a universal dynamical crossover from DLA (the unstable fixed point) to an advection-dominated stable fixed point, since $\mathrm{Pe}(t) \to \infty$. Remarkably, the fractal dimension remains constant during the transition, equal to the value for DLA, in spite of dramatic changes in the growth rate and morphology (as indicated by higher Laurent coefficients). Moreover, the shape of the "average" ADLA cluster in the high-Pe regime of Fig. 11 is quite similar (but not identical) to the exact solution, Eq. (40), for the analogous continuous problem in Fig. 7. Much remains to be done to understand these kinds of models and apply them to materials problems.

4. Curved Surfaces

Entov and Etingof (44) considered the generalized problem of Hele–Shaw flows in a non-planar cell having non-zero curvature. In such problems, the velocity of the viscous flow is still the (surface) gradient of a potential, ϕ, but this function is now a solution of the so-called *Laplace–Beltrami equation* on the curved surface. The Riemann mapping theorem extends to curved surfaces and says that any simply-connected smooth surface is conformally equivalent to the unit disk, the complex plane, or the Riemann sphere. A common example is the well-known *stereographic projection* of the surface of a sphere to the (compactified) complex plane. Under a conformal mapping, solutions of the Laplace–Beltrami equation map to solutions to Laplace's equation and this combination of facts led Entov and Etingof (44) [59] to identify classes of explicit solutions to the continuous Hele–Shaw problem in a variety of non-planar cells. With very similar intent, Parisio *et al.* [60] have recently considered the evolution of Saffman–Taylor fingers on the surface of a sphere.

By now, the reader may realize that most of the methods already considered in this article are, in principle, amenable to generalization to curved surfaces, which can be reached by conformal mapping of the plane. For example, Fig. 12 shows a simulation of a DLA cluster growing on the surface of a sphere, using a generalized Hastings–Levitov algorithm, which takes surface curvature into account. The key modification is to multiply the Jacobian in Eq. (47) by the Jacobian of the stereographic projection, $1 + |z/R|^2$, where R is the radius of the sphere.

It should also be clear that any continuous or discrete growth model driven by a conformally-invariant bulk field, such as ADLA, can be simulated on general curved surfaces by means of appropriate conformal projection to a complex plane. The reason is that the system of Eq. (35) is invariant under any conformal mapping, to a flat or curved surface, because each term transforms

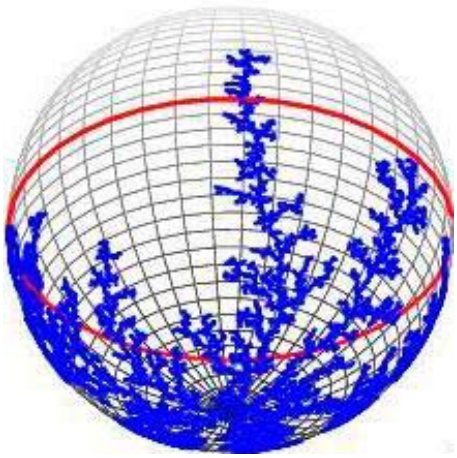

Figure 12. Conformal-mapping simulation of DLA on a sphere. Particles diffuse one by one from the North Pole and aggregate on a seed at a South Pole. (Courtesy of Jaehyuk Choi, Martin Bazant, and Darren Crowdy.)

like the Laplacian, $\nabla^2\phi \to J\nabla^2\phi$, where J is the Jacobian. The purpose of studying these models is not only to understand growth on a particular ideal shape, such as a sphere, but more generally to explore the effect of local surface curvature on pattern formation. For example, this could help interpret mineral deposit patterns in rough geological fracture surfaces, which form by the diffusion and advection of oxygen in slowly flowing water.

5. Outlook

Although conformal mapping has been with us for centuries, new developments with applications continue to the present day. This appears to be the first pedagogical review of stochastic conformal-mapping methods for interfacial dynamics, which also covers the latest progress in continuum methods. Hopefully, this will encourage the further exchange of ideas (and people) between the two fields. Our focus has also been on materials problems, which provide many opportunities to apply and extend conformal mapping.

Building on specific open questions scattered throughout the text, we close with a general outlook on directions for future research. A basic question for both stochastic and continuum methods is the effect of geometrical constraints, such as walls or curved surfaces, on interfacial dynamics. Most work to date has been for either radial or channel geometries, but it would be interesting to describe finite viscous fingers or DLA clusters growing near walls of various shapes, as is often the case in materials applications.

The extension of conformal-map dynamics to multiply connected domains is another mathematically challenging area, which has received some attention recently but seems ripe for further development. Understanding the exact solution structure of Laplacian-growth problems using the mathematical abstraction of quadrature domain theory holds great potential, especially given that mathematicians have already begun to explore the extent to which the various mathematical concepts extend to higher-dimensions [27]. Describing multiply connected domains could pave the way for new mathematical theories of evolving material microstructures. Topology is the main difference between an isolated bubble and a dense sintering compact. Microstructural evolution in elastic solids may be an even more interesting, and challenging, direction for conformal-mapping methods.

From a mathematical point of view, much remains to be done to place stochastic conformal-mapping methods for interfacial dynamics on more rigorous ground. This has recently been achieved in the simpler case of Stochastic Loewner evolution (SLE), which has a similar history to the interfacial problems discussed here [61]. Oded Schramm introduced SLE in 2000 as a stochastic version of the continuous Loewner evolution from univalent function theory, which grows a one-dimensional random filament from a disk or half plane. This important development in pure mathematics came a few years after the pioneering DLA papers of Hastings and Levitov in physics. A notable difference is that SLE has a rigorous mathematical theory based on stochastic calculus, which has enabled new proofs on the properties of percolation clusters and self-avoiding random walks (in two dimensions, of course). One hopes that someday DLA, DBM, ADLA, and other fractal-growth models will also be placed on such a rigorous footing.

Returning to materials applications, it seems there are many new problems to be considered using conformal mapping. Relatively little work has been done so far on void electromigration, viscous sintering, solid pore evolution, brittle fracture, electrodeposition, and solidification in fluid flows. The reader is encouraged to explore these and other problems using a powerful mathematical tool, which deserves more attention in materials science.

References

[1] R.V. Churchill and J.W. Brown, *Complex Variables and Applications*, 5th edn., McGraw-Hill, New York, 1990.

[2] T. Needham, *Visual Complex Analysis*, Clarendon Press, Oxford, 1997.

[3] S.D. Howison, "Complex variable methods in Hele-Shaw moving boundary problems," *Euro. J. Appl. Math.*, 3, 209–224, 1992.

[4] L.M. Cummings, Y.E. Hohlov, S.D. Howison, and K. Kornev, "Two-dimensional soldification and melting in potential flows," *J. Fluid Mech.*, 378, 1–18, 1999.

[5] P.G. Saffman and G.I. Taylor, "The penetration of a fluid into a porous medium or Hele–Shaw cell containing a more viscous liquid," *Proceedings of the Royal Society, London A*, 245, 312–329, 1958.
[6] M. Kruskal and H. Segur, "Asymptotics beyond all orders in a model of crystal growth," *Stud. Appl. Math.*, 85, 129, 1991.
[7] S. Tanveer, "Evolution of Hele–Shaw interface for small surface tension," *Philosophical Transactions of the Royal Society of London A*, 343, 155–204, 1993a.
[8] S. Tanveer, "Surprises in viscous fingering," *J. Fluid Mech.*, 409, 273–308, 2000.
[9] B. Bensimon and D. Shraiman, "Singularities in non-local interface dynamics," *Phys. Rev. A*, 30, 2840–2842, 1984.
[10] L.P. Kadanoff, "Exact solutions for the Saffman–Taylor problem with surface tension," *Phys. Rev. Lett.*, 65, 2986–2988, 1990.
[11] D. Crowdy, "Hele–Shaw flows and water waves," *J. Fluid Mech.*, 409, 223–242, 2000.
[12] J.W. Maclean and P.G Saffman, "The effect of surface tension on the shape of fingers in the Hele–Shaw cell," *J. Fluid Mech.*, 102, 455, 1981.
[13] W.-S. Dai, L.P. Kadanoff, and S.-M. Zhou, "Interface dynamics and the motion of complex singularities," *Phys. Rev. A*, 43, 6672–6682, 1991.
[14] A. Bunde and S. Havlin (ed.), *Fractals and Disordered Systems*, 2nd edn., Springer, New York, 1996.
[15] S. Tanveer, "Singularities in the classical Rayleigh–Taylor flow: formation and subsequent motion," *Proceedings of the Royal Society, A*, 441, 501–525, 1993b.
[16] V.E. Zakharov, "Stability of periodic waves of finite amplitude on the surface of deep fluid," *J. Appl. Mech. Tech. Phys.*, 2, 190, 1968.
[17] T. Yoshikawa and A.M. Balk, "The growth of fingers and bubbles in the strongly nonlinear regime of the Richtmyer–Meshkov instability," *Phys. Lett. A*, 251, 184–190, 1999.
[18] W. Wang, Z. Suo, and T.-H. Hao, "A simulation of electromigration-induced transgranular slits," *J. Appl. Phys.*, 79, 2394–2403, 1996.
[19] M. Ben Amar, "Void electromigration as a moving free-boundary value problem," *Physica D*, 134, 275–286, 1999.
[20] P. Saffman, "Exact solutions for the growth of fingers from a flat interface between two fluids in a porous medium," *Q. J. Mech. Appl. Math.*, 12, 146–150, 1959.
[21] S. Howison, "Fingering in Hele–Shaw cells," *J. Fluid Mech.*, 12, 439–453, 1986.
[22] D. Crowdy and S. Tanveer, "The effect of finiteness in the Saffman–Taylor viscous fingering problem," *J. Stat. Phys.*, 114, 1501–1536, 2004.
[23] S. Richardson, "Hele–Shaw flows with a free boundary produced by the injection of fluid into a narrow channel," *J. Fluid Mech.*, 56, 609–618, 1981.
[24] G. Carrier, M. Krook, and C. Pearson, *Functions of a Complex Variable*, McGraw–Hill, New York, 1966.
[25] S. Richardson, "Hele–Shaw flows with time-dependent free boundaries involving injection through slits," *Stud. Appl. Math.*, 87, 175–194, 1992.
[26] A. Varchenko and P. Etingof, *Why the Boundary of a Round Drop Becomes a Curve of Order Four*, University Lecture Series, AMS, Providence, 1992.
[27] H. Shapiro, *The Schwarz Function and its Generalization to Higher dimension*, Wiley, New York, 1992.
[28] S. Richardson, "Hele–Shaw flows with time-dependent free boundaries involving a multiply-connected fluid region," *Eur. J. Appl. Math.*, 12, 571–599, 2001.
[29] D. Crowdy and J. Marshall, "Constructing multiply-connected quadrature domains," *SIAM J. Appl. Math.*, 64, 1334–1359, 2004.

[30] N. Muskhelishvili, *Some Basic Problems of the Mathematical Theory of Elasticity*, Noordhoff, Groningen, Holland, 1953.
[31] G.K. Batchelor, *An Introduction to Fluid Dynamics*, Cambridge University Press, 1967.
[32] R. Hopper, "Plane stokes flow driven by capillarity on a free surface," *J. Fluid Mech.*, 213, 349–375, 1990.
[33] D. Crowdy, "A note on viscous sintering and quadrature identities," *Eur. J. Appl. Math.*, 10, 623–634, 1999.
[34] D.G. Crowdy, "Viscous sintering of unimodal and bimodal cylindrical packings with shrinking pores," *Eur. J. Appl. Math.*, 14, 421–445, 2003.
[35] S. Richardson, "Plane stokes flow with time-dependent free boundaries in which the fluid occupies a doubly-connected region," *Eur. J. Appl. Math.*, 11, 249–269, 2000.
[36] W. Wang and Z. Suo, "Shape change of a pore in a stressed solid via surface diffusion motivated by surface and elastic energy variations," *J. Mech. Phys. Solids*, 45, 709–729, 1997.
[37] M.Z. Bazant, "Conformal mapping of some non-harmonic functions in transport theory," *Proceedings of the Royal Society, A*, 460, 1433, 2004.
[38] M.Z. Bazant, J. Choi, and B. Davidovitch, "Dynamics of conformal maps for a class of non-Laplacian growth phenomena," *Phys. Rev. Lett.*, 91, 045503, 2003.
[39] K. Kornev and G. Mukhamadullina, "Mathematical theory of freezing for flow in porous media," *Proceedings of the Royal Society, London A*, 447, 281–297, 1994.
[40] J. Choi, D. Margetis, T.M. Squires, and M.Z. Bazant, "Steady advection-diffusion to finite absorbers in two-dimensional potential flows," *J. Fluid Mech.*, 2004b.
[41] J. Choi, B. Davidovitch, and M.Z. Bazant, "Crossover and scaling of advection-diffusion-limited aggregation," In preparation, 2004a.
[42] M.B. Hastings and L.S. Levitov, "Laplacian growth as one-dimensional turbulence," *Physica D*, 116, 244–252, 1998.
[43] B. Davidovitch, H.G.E. Hentschel, Z. Olami, I. Procaccia, L.M. Sander, and E. Somfai, "Diffusion-limited aggregation and iterated conformal maps," *Phys. Rev. E*, 59, 1368–1378, 1999.
[44] P.L. Duren, *Univalent Functions*, Springer-Verlag, New York, 1983.
[45] M.B. Hastings, "Renormalization theory of stochastic growth," *Phys. Rev. E*, 55, 135, 1997.
[46] T.A. Witten and L.M. Sander, "Diffusion-limited aggregation: a kinetic critical phenomenon," *Phys. Rev. Lett.*, 47, 1400–1403, 1981.
[47] T.C. Halsey, "Diffusion-limited aggregation: a model for pattern formation," *Phys. Today*, 53, 36, 2000.
[48] M.G. Stepanov and L.S. Levitov, "Laplacian growth with separately controlled noise and anisotropy," *Phys. Rev. E*, 63, 061102, 2001.
[49] M.H. Jensen, A. Levermann, J. Mathiesen, and I. Procaccia, "Multifractal structure of the harmonic measure of diffusion-limited aggregates," *Phys. Rev. E*, 65, 046109, 2002.
[50] R.C. Ball and E. Somfai, "Theory of diffusion controlled growth," *Phys. Rev. Lett.*, 89, 133503, 2002.
[51] E. Somfai, L.M. Sander, and R.C. Ball, "Scaling and crossovers in diffusion limited aggregation," *Phys. Rev. Lett.*, 83, 5523, 1999.
[52] E. Somfai, R.C. Ball, J.P. DeVita, and L.M. Sander, "Diffusion-limited aggregation in channel geometry," *Phys. Rev. E*, 68, 020401, 2003.
[53] F. Barra, B. Davidovitch, and I. Procaccia, "Iterated conformal dynamics and Laplacian growth," *Phys. Rev. E*, 65, 046144, 2002a.

[54] A. Levermann and I. Procaccia, "Algorithm for parallel laplacian growth by iterated conformal maps," *Phys. Rev. E*, 69, 031401, 2004.
[55] L. Niemeyer, L. Pietronero, and H.J. Wiesmann, "Fractal dimension of dielectric breakdown," *Phys. Rev. Lett.*, 52, 1033–1036, 1984.
[56] M.B. Hastings, "Fractal to nonfractal phase transition in the dielectric breakdown model," *Phys. Rev. Lett.*, 87, 175502, 2001.
[57] H.J. Hermann and S. Roux (eds.), *Statistical Models for the Fracture of Disordered Media*, North-Holland, Amsterdam, 1990.
[58] F. Barra, A. Levermann, and I. Procaccia, "Quasistatic brittle fracture in inhomogeneous media and iterated conformal maps," *Phys. Rev. E*, 66, 066122, 2002b.
[59] V.M. Entov and P.I. Etingof, "Bubble contraction in Hele–Shaw cells," *Quart. J. Mech. Appl. Math.*, 507–535, 1991.
[60] F. Parisio, F. Moreas, J.A. Miranda, and M. Widom, "Saffman–Taylor problem on a sphere," *Phys. Rev. E*, 63, 036307, 2001.
[61] W. Kager and B. Nienhuis, "A guide to stochastic loewner evolution and its applications," *J. Stat. Phys.*, 115, 1149–1229, 2004.

Author Query

1. Figures[1, 7, 8, 11, 12] are in color.